



## Flow stress and dynamic recrystallization behavior of Al–9Mg–1.1Li–0.5Mn alloy during hot compression process

Xi-hong CHEN<sup>1,2</sup>, Cai-he FAN<sup>1</sup>, Ze-yi HU<sup>1</sup>, Jian-jun YANG<sup>1</sup>, Wen-li GAO<sup>3</sup>

1. College of Metallurgy and Material Engineering, Hunan University of Technology, Zhuzhou 412007, China;

2. CRRC Zhuzhou Electric Locomotive Co., Ltd., Zhuzhou 412004, China;

3. College of Materials Science and Engineering, Hunan University, Changsha 410082, China

Received 16 January 2018; accepted 23 July 2018

**Abstract:** The flow stress behavior of spray-formed Al–9Mg–1.1Li–0.5Mn alloy was studied using thermal simulation tests on a Gleeble–3500 machine over deformation temperature range of 300–450 °C and strain rate of 0.01–10 s<sup>−1</sup>. The microstructural evolution of the alloy during the hot compression process was characterized by transmission electron microscopy (TEM) and electron back scatter diffractometry (EBSD). The results show that the flow stress behavior and microstructural evolution are sensitive to deformation parameters. The peak stress level, steady flow stress, dislocation density and amount of substructures of the alloy increase with decreasing deformation temperature and increasing strain rate. Conversely, the high angle grain boundary area increases, the grain boundary is in serrated shape and the dynamic recrystallization in the alloy occurs. The microstructure of the alloy is fibrous-like and the main softening mechanism is dynamic recovery during steady deformation state. The flow stress behavior can be represented by the Zener–Hollomon parameter  $Z$  in the hyperbolic sine equation with the hot deformation activation energy of 184.2538 kJ/mol. The constitutive equation and the hot processing map were established. The hot processing map exhibits that the optimum processing conditions for Al–9Mg–1.1Li–0.5Mn alloy are in deformation temperature range from 380 to 450 °C and strain rate range from 0.01 to 0.1 s<sup>−1</sup>.

**Key words:** Al–9Mg–1.1Li–0.5Mn alloy; flow stress; constitutive equation; processing map; dynamic recrystallization

### 1 Introduction

The Al–Mg–Li alloy has excellent properties such as corrosion resistance, weldability, moderate strength and low cost, which makes it an attractive material in automotive, shipping and aerospace industry [1–3].

However, it is difficult to obtain high-strength and high-toughness by conventional casting method [4] due to the coarse grain and dendrite segregation caused by the low cooling rate. Spray forming technology is recognized as an ideal method to prepare high Mg content Al–Mg–Li alloy with high cooling rate, high level of solute Mg, fine grains as well as no macro segregation of alloy composition, which can compensate the deficiencies of the casting method [5]. Compared with the as-cast alloy ingot, however, the hot-compression deformation of the spray forming alloy is more difficult due to the high solute Mg content in the

Al–Mg alloy [6]. It is very significant to establish the reasonable processing and basic parameters before plastic processing (e.g. the flow stress) [7,8]. In recent years, many researchers [9–11] have reported the flow stress behavior of Al–Mg alloys during hot compression process. JOBBA et al [9] investigated the flow stress and work-hardening behavior of Al–Mg alloys and reported that the flow stress was a significant influencing factor for plastic deformation capacity of cast-state Al–Mg alloy. SHEIKH and SERAJZADEH [10] investigated the effect of flow stress on the plastic deformation behavior of cast-state AA5083 alloy by establishing model. WANG et al [11] researched the flow stress behavior of spray-formed 5A06 aluminum alloy during hot compression process. However, all these reports are focused on flow stress behavior of low Mg content Al–Mg alloy, and little reports are on high Mg content, especially high Mg content spray-formed Al–Mg–Li alloy.

In this work, we carry out an isothermal hot compression test on Gleeble–3500 machine to investigate the flow stress behavior of spray-formed Al–9Mg–1.1Li–0.5Mn alloy in a wide range of strain, deformation temperature and strain rate. The quantitative relationship between flow stress and the deformation parameters is explored to establish the constitutive equation and hot processing map of the alloy. The interactive influence between microstructural evolution and processing conditions at elevated temperature is also studied.

## 2 Experimental method and processing map principles

### 2.1 Experimental method

The spray forming preform of Al–9Mg–1.1Li–0.5Mn alloy was produced by a self-developed spray forming machine (SD380). The chemical composition of the deposit preform is as follows: 9.0% Mg, 1.1% Li, 0.5% Mn and 91.5% Al (mass fraction). The aluminum alloy was firstly melted in a graphite crucible at 1053 K. To avoid oxidization, the melting and refining processes were protected with N<sub>2</sub>. As the refining process was finished, the temperature was increased to 1103 K, and the aluminum alloy melt was drained into the preheated graphite crucible. The alloy melt in the crucible flowed through the delivery tube with the inner diameter of 3–5 mm and atomized in an atomizer. the pressure of N<sub>2</sub> is 0.5–1.5 MPa. The distance between the deposited layer and the atomizer is 100–250 mm. The plate with cross section of 12 mm × 100 mm used in this work was extruded (using 1250 t extruder) from the preform at extrusion temperature of 450 °C and extrusion ratio of 15:1. The microstructure of the as-extruded plate is shown in Fig. 1. It can be seen that the microstructure of the plate exhibits a strip-like structure with coarse grains. All the compression-testing specimens of 8 mm in diameter and 12 mm in height were machined with their cylinder axes perpendicular to the surface of the plate materials.

Isothermal and constant strain rate compression tests were carried out on a Gleeble–3500 testing system at temperatures of 300, 350, 400 and 450 °C and strain rates of 0.01, 0.1, 1, 5 and 10 s<sup>-1</sup>. Before hot compression tests, the specimens were heated to the deformation temperature at the heating rate of 5 °C/s and held for 3 min under isothermal conditions so as to obtain the uniform deformation temperature, and then hot compressed to a true strain of 0.8. At both ends of the cylinder sample, the lubricant was daubed with the chemical component of 75% graphite, 20% engine oil and 5% nitric acid from mesitylene fat. After the compression test, the specimens were water quenched

with delay time less than 5 s to maintain the hot-deformed microstructures for optical observation. Transmission electron microscopy (Titan G2 60-300 TEM) and electron backscatter diffraction (EBSD, Helios Nanolab 600i-SEM) were employed to characterize the microstructural evolution of the deformed specimen. The samples for TEM and EBSD observation were prepared on sections parallel to the compression axis. The specimens were prepared by the standard twin-jet electro-polishing method using 67% CH<sub>3</sub>OH and 33% HNO<sub>3</sub> acid at –30 °C. Similarly, the EBSD samples were prepared by electro-polishing method at –30 °C, using a solution of 80% C<sub>2</sub>H<sub>5</sub>OH and 20% HClO<sub>4</sub> at 20 V for 30 s. The EBSD samples were analyzed by TSL OIM software, performed at 20 kV and 70 ° tilt with 0.2 μm scan step.

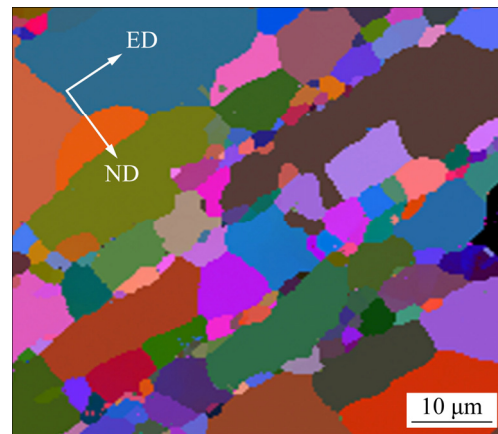


Fig. 1 EBSD map of Al–9Mg–1.1Li–0.5Mn alloy extruded at 450 °C

### 2.2 Processing map principles

Processing maps developed on the basis of the dynamic materials model (DMM) by PRASAD et al [12] and GEGEL and DORAIVELU [13] were used to study the deformation behavior of the alloy plate at elevated temperature. This model can not only associate deformable media mechanics and the microstructural evolution of dissipative structure, but also successfully describe the dynamic response area of the materials in the hot compression process. In this model, the materials under hot compression conditions are considered to a power dissipater ( $P$ ), divided into two parts of  $G$  consumption constant and  $J$  consumption co-content, which is given as follows:

$$P = \sigma \dot{\epsilon} = G + J = \int_0^{\dot{\epsilon}} \sigma d\dot{\epsilon} + \int_0^{\sigma} \dot{\epsilon} d\sigma \quad (1)$$

$G$  and  $J$  are given by

$$G = \int_0^{\dot{\epsilon}} \sigma d\dot{\epsilon} \quad (2)$$

$$J = \int_0^{\sigma} \dot{\epsilon} d\sigma \quad (3)$$

where  $G$  is the energy consumed by plastic deformation and  $J$  is the energy consumed by microstructural evolution. The distribution between  $G$  and  $J$  is determined by the strain rate sensitivity exponent  $m$ . While for the nonlinear dissipation, the power dissipation characteristics of the material can be reflected by power dissipation efficiency  $\eta$  [13], which is given by

$$\eta = \frac{J}{J_{\max}} = \frac{2m}{m+1} \quad (4)$$

### 3 Results and discussion

#### 3.1 Flow behavior

Figure 2 shows a series of true stress–true strain curves of the as-extruded plate of the Al–9Mg–1.1Li–0.5Mn alloy compressed at 300–450 °C and various strain rates. It can be seen that the flow stress curves exhibit the similar characteristics in general at the early stage of the deformation process. The flow stress presents a sharp increase until a peak stress at a quite small strain only with some subtle differences. As shown in Fig. 2, at the lowest stress rate ( $\dot{\epsilon}=0.01 \text{ s}^{-1}$ ), all the

true stress–true strain curves at deformation temperature from 350 to 450 °C have an obvious stress peak, which exhibit initial flow softening on reaching a single peak stress. With the stress rate increasing, the obvious stress peak can be only observed at higher deformation temperature, and the peak can be observed until the temperature is up to 450 °C at the stress rate of  $5 \text{ s}^{-1}$  (Fig. 2(d)). It is interesting to note that serrations are observed on the true stress–true strain curves in Figs. 2(c) and 2(d). This is mainly attributed to the rapid increase of the dislocation density during the early stages of the deformation process. On one hand, the flow stress increases sharply with the increase of the strain, which leads to the work hardening of the alloy. On the other hand, with continuous increasing of deformation, the dynamic recovery and crystallization take place, which will soften the alloy. Such serrated yielding behavior is attributed to the dynamic strain ageing effect [8,14]. In a word, it can be seen from Fig. 2 that the flow behaviors of the experimental alloy are greatly influenced by deformation temperature, strain rate as well as true strain. This phenomenon is similar with that reported by WANG et al [11] and CAO et al [15].

The effect of deformation temperatures and strain rates on peak flow stress of Al–9Mg–1.1Li–0.5Mn alloy

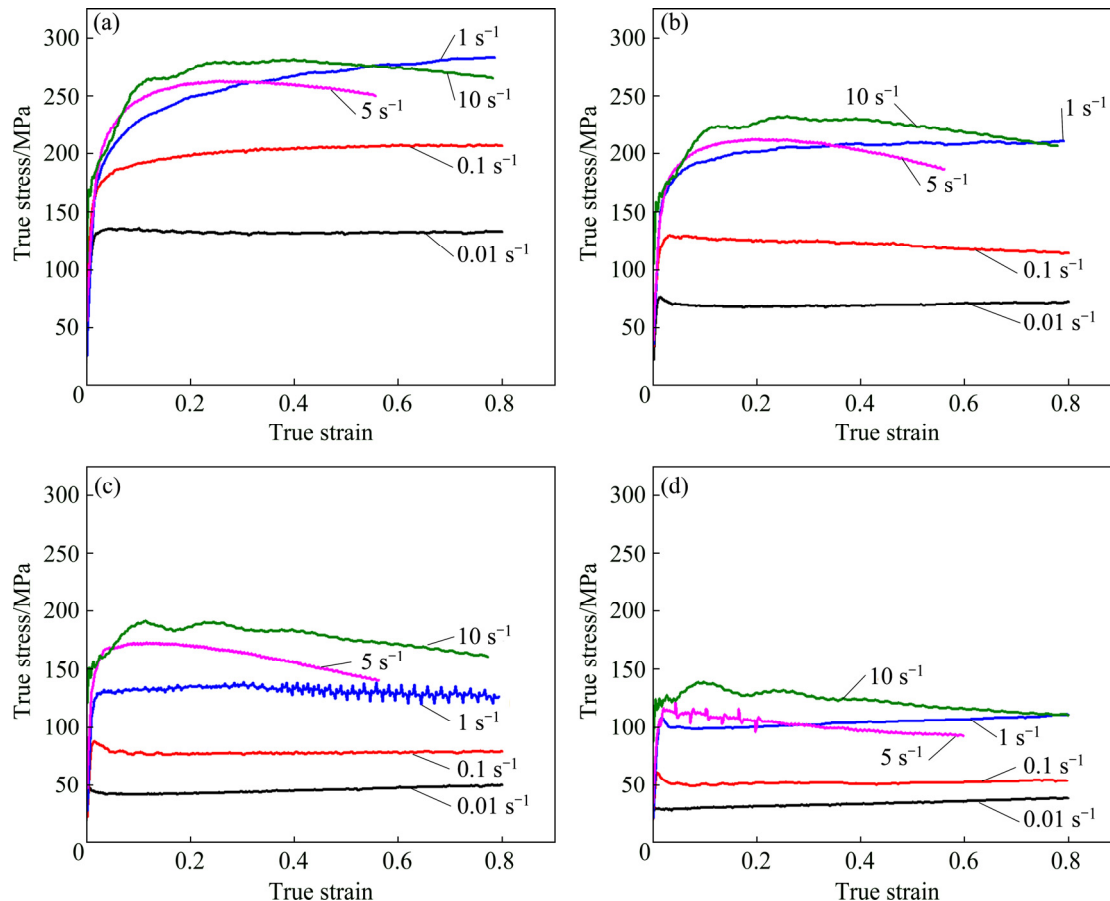


**Fig. 2** True stress–true strain curves of Al–9Mg–1.1Li–0.5Mn alloy at various strain rates and different decomposition temperatures: (a) 300 °C; (b) 350 °C; (c) 400 °C; (d) 450 °C

is shown in Fig. 3. It can be obviously found that the peak flow stress is sensitive to deformation temperature and strain rate. The peak flow stress decreases as deformation temperature increases or strain rate decreases. At low deformation temperature and high strain rate, the dynamic recovery or recrystallization is restrained. This is because the mobility of dislocation is put off, and there is no sufficient time for energy accumulation and dislocation annihilation. However, at high deformation temperature and low strain rate, the average kinetic energy of metal atoms accumulates, which can improve the dislocation mobility. Therefore, the dynamic recovery or dynamic recrystallization may occur and the peak flow stress will decrease.

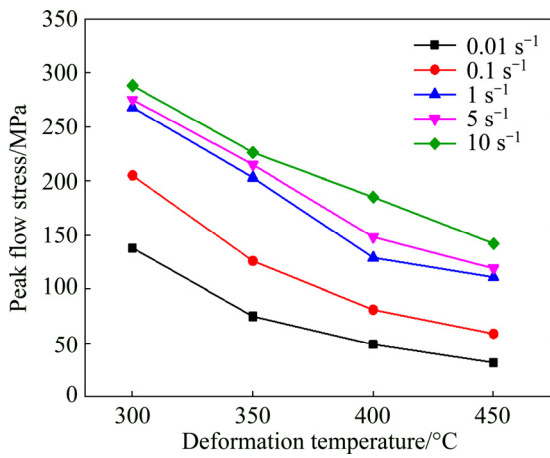


Fig. 3 Peak flow stress in hot compression of experimental alloy under different deformation conditions

### 3.2 Constitutive equation

The Arrhenius equation is widely used to describe the relationship among flow stress, strain rate and temperature under hot deformation conditions [16,17]. There are three forms of the flow stress function as follows:

$$\dot{\varepsilon} = A_1 \sigma^{n_1} \exp\left(\frac{-Q}{RT}\right) \quad (\alpha\sigma < 0.8) \quad (5)$$

$$\dot{\varepsilon} = A_2 \exp(\beta\sigma) \exp\left(\frac{-Q}{RT}\right) \quad (\alpha\sigma > 1.2) \quad (6)$$

$$\dot{\varepsilon} = A[\sinh(\alpha\sigma)]^n \exp\left(\frac{-Q}{RT}\right) \quad (7)$$

where  $\alpha$ ,  $n$ ,  $\beta$ ,  $A$ ,  $A_1$  and  $A_2$  are constants:  $\alpha$  (MPa<sup>-1</sup>) ( $\alpha = \beta/n$ ) is the parameter of the stress level;  $n$  is the stress exponent;  $A$ ,  $A_1$  and  $A_2$  (s<sup>-1</sup>) are structure factors.  $\sigma$  (MPa) is the flow stress;  $\dot{\varepsilon}$  (s<sup>-1</sup>) is the strain rate;  $T$  (K) is the deformation temperature;  $Q$  (J/m) is an activation energy for deformation. The power law (Eq. (5)) and the exponential law (Eq. (6)) are suitable for a low stress and a high stress, respectively. The hyperbolic-sine equation (Eq. (7)) has been widely applied to describing

the deformation parameters in a wide range of stresses [18–20].

In the present work, the relationships between peak flow stress and strain rate are obtained.  $n_1$  and  $\beta$  are calculated from the slopes of the plots of  $\ln \dot{\varepsilon} - \ln \sigma$  and  $\ln \dot{\varepsilon} - \sigma$ , as shown in Figs. 4(a) and (b).

It was also proposed that the flow stress behavior can be represented by the Zener-Hollomon parameter  $Z$  in the hyperbolic sine equation [6,16,18]. The equation is given as follows:

$$Z = \dot{\varepsilon} \exp\left(\frac{Q}{RT}\right) \quad (8)$$

Then, putting Eq. (7) into Eq. (8) yields

$$Z = \dot{\varepsilon} \exp\left(\frac{Q}{RT}\right) = A[\sinh(\alpha\sigma)]^n \quad (9)$$

Taking the natural logarithm of both sides of Eq. (9) and Eq. (7) and derivation, we can obtain

$$\ln \dot{\varepsilon} = \ln A - Q/(RT) + n \ln[\sinh(\alpha\sigma)] \quad (10)$$

And then, the deformation activation energy  $Q$  can be expressed by

$$Q = nR \left. \frac{\partial \ln[\sinh(\alpha\sigma)]}{\partial(1/T)} \right|_{\dot{\varepsilon}} = R \left. \frac{\partial \ln \dot{\varepsilon}}{\partial \ln[\sinh(\alpha\sigma)]} \right|_T \cdot \left. \frac{\partial \ln[\sinh(\alpha\sigma)]}{\partial(1/T)} \right|_{\dot{\varepsilon}} \quad (11)$$

$$K = \frac{\partial \ln[\sinh(\alpha\sigma)]}{\partial(1/T)} = \frac{Q}{nR} \quad (12)$$

where  $n$  is the mean slope of the  $\ln \dot{\varepsilon} - \ln[\sinh(\alpha\sigma)]$  plots at different temperatures and  $K$  is the mean slope of  $\ln[\sinh(\alpha\sigma)] - 1/T$  plots at various strain rates, as shown in Figs. 4(c) and (d).

Taking the natural logarithm of both sides of Eq. (9) and derivation, we can obtain

$$\ln Z = \ln \dot{\varepsilon} + \frac{Q}{RT} = \ln A + n \ln[\sinh(\alpha\sigma)] \quad (13)$$

Figure 5 shows the relationship between  $\ln Z$  and  $\ln[\sinh(\alpha\sigma)]$  of the experimental alloy. The material constants of the alloy obtained from the experimental data are listed in Table 1. By substitution of the above values into Eq. (7), the constitutive equation of Al–9Mg–1.1Li–0.5Mn alloy is obtained and shown as follows:

$$\dot{\varepsilon} = 1.2029 \times 10^{10} [\sinh(0.0134\sigma)]^{4.3928} \exp\left(\frac{-184253.8}{RT}\right) \quad (14)$$

### 3.3 Processing maps and microstructural evolution

The processing maps of the as-extruded Al–9Mg–1.1Li–0.5Mn alloy at strain of 0.1 and 0.3 are shown in

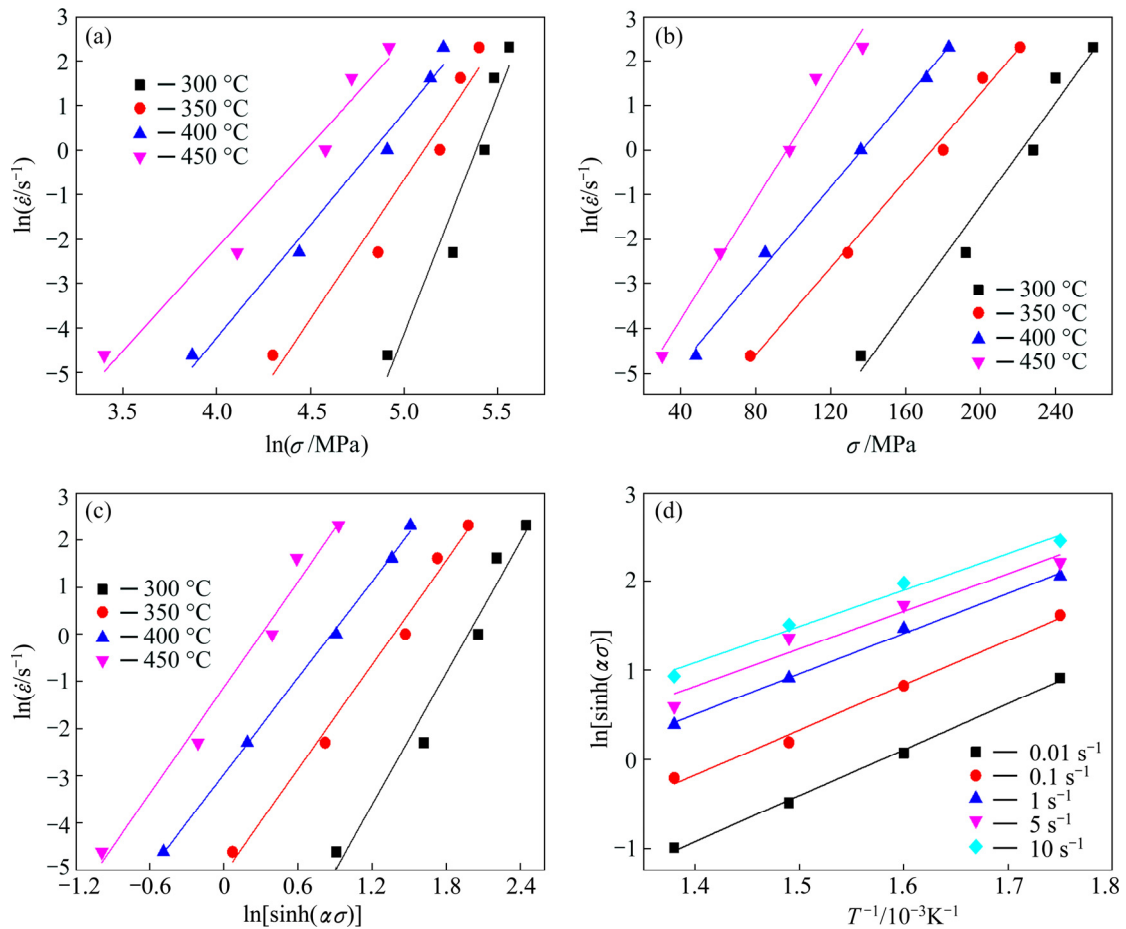


Fig. 4 Relationship among  $\dot{\epsilon}$ ,  $\sigma$ ,  $\ln \dot{\epsilon}$ ,  $1/T$  and  $\ln[\sinh(\alpha\sigma)]$ : (a)  $\ln \dot{\epsilon} - \ln \sigma$ ; (b)  $\ln \dot{\epsilon} - \sigma$ ; (c)  $\ln \dot{\epsilon} - \ln[\sinh(\alpha\sigma)]$ ; (d)  $\ln[\sinh(\alpha\sigma)] - 1/T$

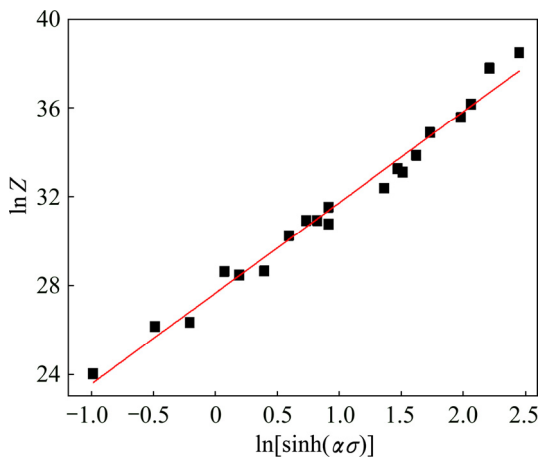


Fig. 5 Relationship between  $\ln Z$  and  $\ln[\sinh(\alpha\sigma)]$

Table 1 Material constants of experimental alloy

Calculation No.	$A/s^{-1}$	$n$	$a/MPa^{-1}$	$Q/(kJ \cdot mol^{-1})$
1	$1.3067 \times 10^{10}$	4.8900	0.0121	210.6522
2	$1.2543 \times 10^{10}$	4.3516	0.0137	186.7743
3	$1.0479 \times 10^{10}$	3.9367	0.0145	155.3349
Average	$1.2029 \times 10^{10}$	4.3928	0.0134	184.2538

Fig. 6. The contours on processing maps represent content efficiency ( $\eta$ ) of power dissipation and gray area represents the instability domains. The other area represents secure processing zone. As shown in Figs. 6(a) and (b), it can be obviously found that the efficiency of power dissipation ( $\eta$ ) decreases with increasing strain rate, and the peak values of power dissipation ( $\eta$ ) is 0.47 and 0.41, respectively. It be seen that the peak values of power dissipation ( $\eta$ ) decreases with increasing strain, which indicates that the strain has a significant effect on the processing maps. Generally, the larger the  $\eta$  is in this zone, the better processing of the material in this deformation condition will be. However, the highest efficiency of power dissipation does not necessarily mean better workability. LI et al [21] found in Al–Si alloy that the optimum processing conditions should be determined by the efficiency of power dissipation and the instability parameter. Many researchers have widely confirmed that the deformation zones with different efficiencies of power dissipation have their homologous deformation mechanism [22]. To investigate the deformation mechanism and optimize process parameters, the microstructures of the spray-forming Al–9Mg–

1.1Li–0.5Mn alloy deformed at a few typical deformation zones are characterized and analyzed.

The TEM images of the Al–9Mg–1.1Li–0.5Mn alloy under different conditions are shown in Fig. 7. As shown in Figs. 7(a) and (b), when  $\dot{\epsilon} = 0.1 \text{ s}^{-1}$ , the dislocation density of the alloy is high, the dislocations tangles zone is large, the size of precipitation phases is big, and as shown from the arrows in Fig. 7, massive

dislocation cell structure can be observed with the size of 10–40 nm. As shown in Figs. 7(c) and (d), when  $\dot{\epsilon}$  is increased from 0.1 to  $0.3 \text{ s}^{-1}$ , the dislocation density is decreased obviously; high-angle grain boundary (HAGB) can be observed clearly; the number of dislocation cells is also decreased obviously. However, the amount of precipitation phases in the alloy is increased obviously and the size of precipitation phases is smaller. So, the

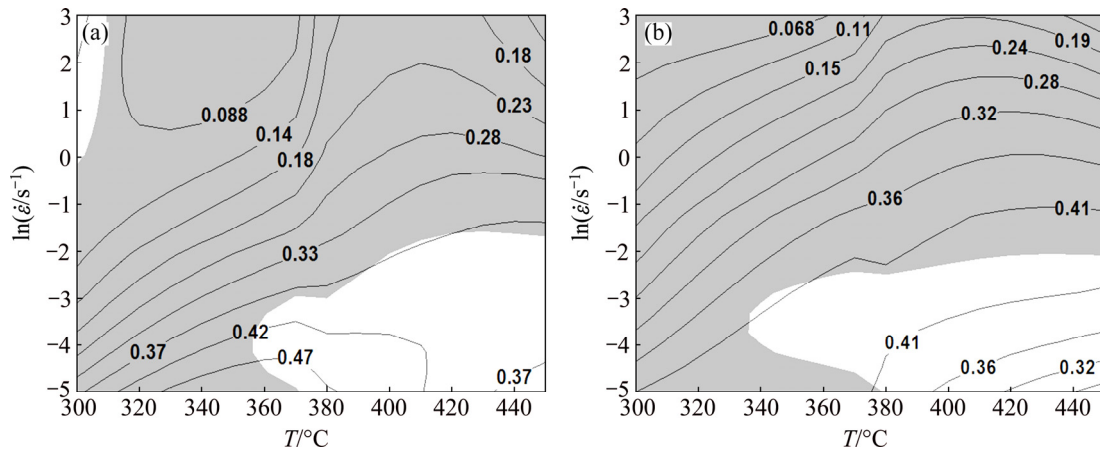


Fig. 6 Hot processing maps of Al–9Mg–1.1Li–0.5Mn alloy under strains of 0.1 (a) and 0.3 (b)

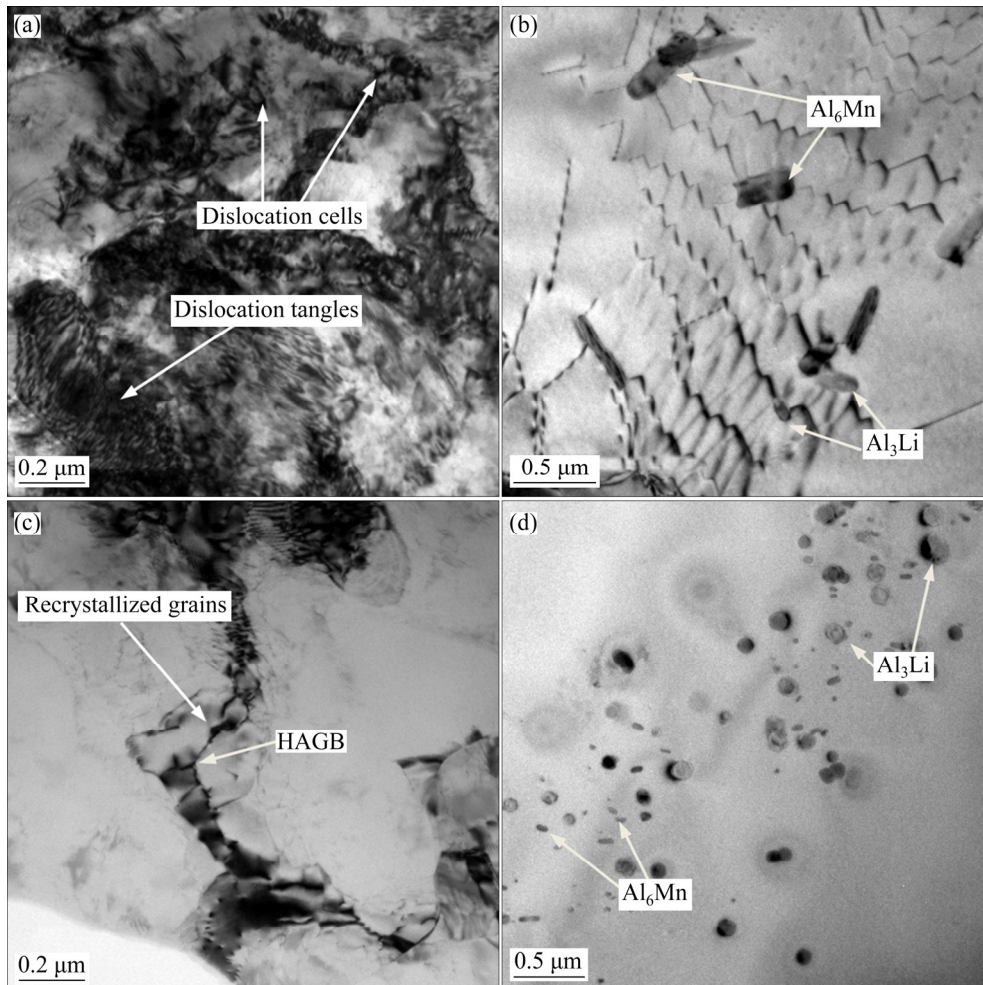
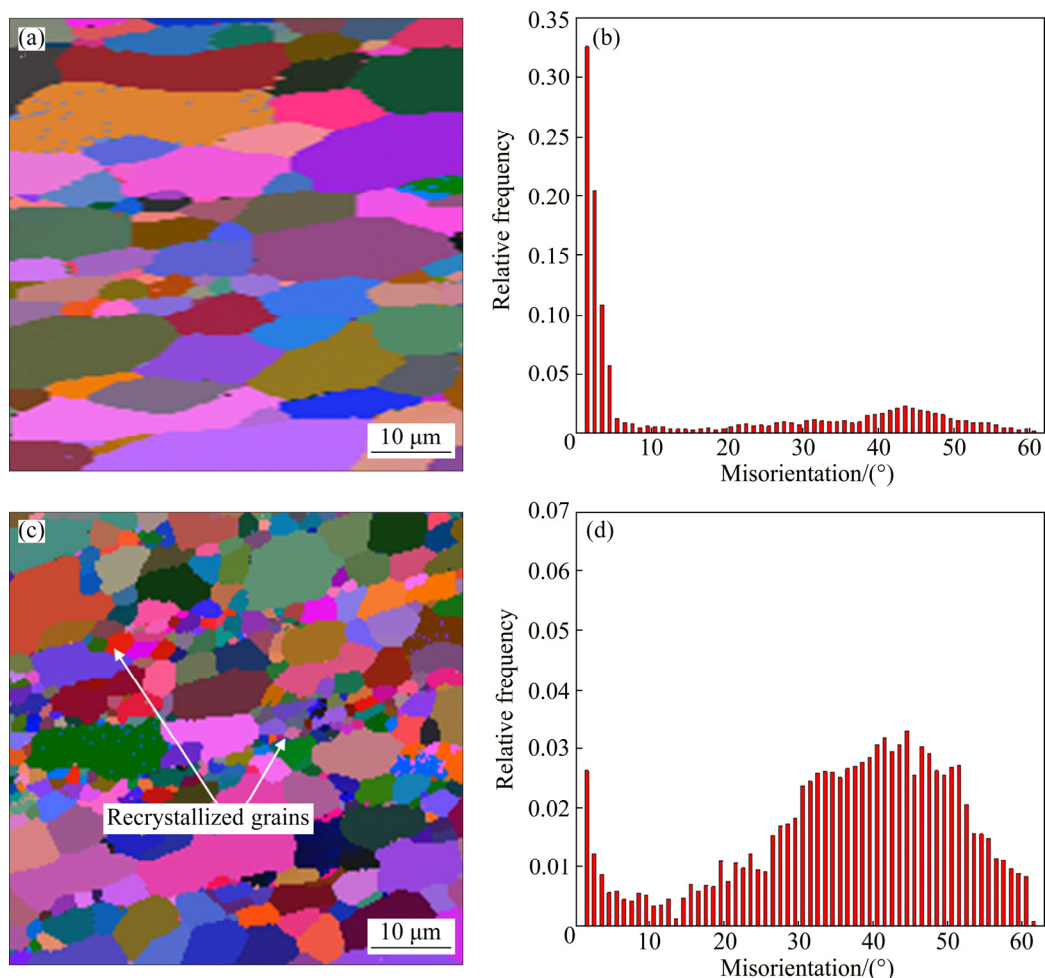


Fig. 7 TEM images of Al–9Mg–1.1Li–0.5Mn alloy under different conditions: (a, b)  $\dot{\epsilon} = 0.1$ ,  $T = 400 \text{ }^{\circ}\text{C}$ ; (c, d)  $\dot{\epsilon} = 0.3$ ,  $T = 400 \text{ }^{\circ}\text{C}$

sample shows recrystallization structure. The HAGB is marked by the arrows in Fig. 7. These indicate that the dynamic recovery is the main softening mechanism at the initial stage during hot compression process. However, because the disappearing number of dislocation in dynamic recovery process is far lower than its new growth number in the hot compression process, work hardening plays the leading role in this alloy. As mentioned in Refs. [23,24], due to small size of the dislocation cell, the recrystallization is incomplete dynamic recrystallization and the softening effect is small. So, at the initial stage during hot deformation process, the strain rate increases sharply with the deformation degree increasing; but when the strain reaches a certain value, the stress–strain curve becomes straight, as shown in Fig. 2(f). In this stage, the deformation of the alloy appears in apparent steady-state flow characteristics and the recrystallization softening and the work hardening of the alloy reach dynamic equilibrium. As reported by ZHA et al [8], the softening of the Al–7Mg alloy is the result of both dynamic recovery and recrystallization during the hot deformation

process.

The EBSD maps of Al–9Mg–1.1Li–0.5Mn alloy at different deformation temperatures and strain rates are shown in Fig. 8. It can be seen from Fig. 8(a) that the origin grain becomes thinner and longer, and fine equiaxed grains can be found when the alloy is compressed at low deformation temperature (300 °C) and high strain rate (10 s<sup>-1</sup>). It is indicated that the main deformation mechanism of Al–9Mg–1.1Li–0.5Mn alloy is dynamic recovery and the full dynamic recrystallization does not occur under this condition. When the hot compression is carried out at high deformation temperature (450 °C) and low strain rate (0.01 s<sup>-1</sup>), as shown in Fig. 8(b), the original grain boundaries appear in serrated shape and the high-angle grain boundaries increase significantly. In addition, numerous fine recrystallized grains can be observed near the grain boundaries, which indicates that the fully dynamic recrystallization occurs under this condition. As mentioned in Ref. [21], at higher deformation temperature and lower strain rate, the diffusion abilities of atoms, cross-slip of dislocation and migration of grain



**Fig. 8** EBSD maps (a, c) and grain orientation distribution diagrams (b, d) of Al–9Mg–1.1Li–0.5Mn alloy under different conditions: (a, b)  $\epsilon=0.3$ ,  $T=300$  °C,  $\dot{\epsilon}=10$  s<sup>-1</sup>; (c, d)  $\epsilon=0.3$ ,  $T=450$  °C,  $\dot{\epsilon}=0.01$  s<sup>-1</sup>

boundaries can be enhanced, and these are beneficial to the nucleation and nucleus growth of dynamic recrystallization. GHOLINIA et al [25] also found in Al–3Mg alloy that the higher deformation temperature or the higher strain lead to dynamic recrystallization more easily. WANG et al [23] confirmed that dynamic recovery is the primary mechanism when the Al–15%Si alloy was deformed at low temperature and high strain rate.

Based on the analysis above, deformation temperature, strain and strain rate show a remarkable effect on dynamic recrystallization. The present work shows that dynamic recrystallization can be effectively induced by optimized processing parameters which can further improve the microstructures of Al–9Mg–1.1Li–0.5Mn alloy. The as-obtained optimum processing conditions are located in deformation temperature range from 380 to 450 °C and strain rate range from 0.01 to 0.1 s<sup>-1</sup> at the strain of 0.3 with higher power efficiency of 32%–41%.

## 4 Conclusions

1) The hot compressive behaviors of Al–9Mg–1.1Li–0.5Mn alloy were studied at the temperature from 300 to 450 °C and the strain rate from 0.01 to 10 s<sup>-1</sup>. The results show that the flow stress and microstructure evolution of the alloy are sensitive to deformation parameters, and the alloy has high work hardening ability. The peak stress level and steady flow stress increase with decreasing deformation temperature and increasing strain rate, which can be represented by the Zener–Hollomon parameter  $Z$  with the hyperbolic sine equation.

2) The constitutive relationship of experimental alloy has been developed to describe deformation temperature and strain rate dependence of the flow stress. The deformation activation energy  $Q$  is calculated to be 184.2538 kJ/mol. The main deformation mechanism of the Al–9Mg–1.1Li–0.5Mn alloy is dynamic recovery and full dynamic recrystallization does not occur under low temperature and high strain rate condition. While under high deformation temperature and low strain rate condition, the fully dynamic recrystallization of the experiment alloy occurs in the hot compression process. The optimum processing conditions for the spray-formed Al–9Mg–1.1Li–0.5Mn alloy are in deformation temperature range from 380 to 450 °C and strain rate range from 0.01 to 0.1 s<sup>-1</sup> at the strain of 0.3 with higher power efficiency of 32%–41%.

## References

[1] LI Hong-ping, YE Ling-ying, ZHANG Pan, ZHONG Jue, HUANG Ming-hui. Microstructure and texture characterization of superplastic

Al–Mg–Li alloy [J]. Transactions of Nonferrous Metals Society of China, 2014, 24: 2079–2087.

[2] PUGACHEVA N B, ANTENOROVA N P, SENAIEVA E I. Study of the structure and properties of laser-welded joints of the Al–Mg–Li alloy [J]. The Physics of Metals and Metallography, 2015, 116(12): 1259–1269.

[3] TOLGA D, COSTAS S. Recent developments in advanced aircraft aluminum alloys [J]. Materials and Design, 2014, 56(2): 862–871.

[4] WANG Xiao-feng, GUO Ming-xing, ZHANG Yan, XING Hui, LI Yong, LUO Jin-ru. The dependence of microstructure, texture evolution and mechanical properties of Al–Mg–Si–Cu alloy sheet on final cold rolling deformation [J]. Journal of Alloys and Compounds, 2016, 657(5): 906–916.

[5] FAN Cai-he, CHEN Xi-hong, ZHOU Xin-peng, OU Ling, YANG Jian-jun, PENG Ying-biao. Microstructure evolution and strengthening mechanisms of spray-formed 5A12 Al alloy processed by high reduction rolling [J]. Transactions of Nonferrous Metals Society of China, 2017, 27(11): 2363–2370.

[6] FAN Cai-he, PENG Ying-biao, YANG Hai-tang, ZHOU Wei, YAN Hong-ge. Hot deformation behavior of Al–9.0Mg–0.5Mn–0.1Ti alloy based on processing maps [J]. Transactions of Nonferrous Metals Society of China, 2017, 27(2): 289–297.

[7] HOGG S C, PALMER I G, THOMAS L G, GRANG P S. Processing, microstructure and property aspects of a spray-cast Al–Mg–Li–Zr alloy [J]. Acta Materialia, 2007, 55: 1885–1894.

[8] ZHA Min, LI Yan-jun, MATHIESEN R H, ROVON H J. Microstructure evolution and mechanical behavior of a binary Al–7Mg alloy processed by equal-channel angular pressing [J]. Acta Materialia, 2015, 84(4): 42–54.

[9] JOBBA M, MISHRA R K, NIEWCZAS M. Flow stress and work-hardening behavior of Al–Mg binary alloys [J]. International Journal of Plasticity, 2015, 65: 43–60.

[10] SHEIKH H, SERAJZADEH S. Estimation of flow stress behavior of AA5083 using artificial neural networks with regard to dynamic strain ageing effect [J]. Journal of Materials Processing Technology, 2008, 196: 115–119.

[11] WANG Zhan-feng, ZHANG Hao, CHEN Zheng-hua. Flow stress behaviors of spray deposited 5A06 aluminum alloy under hot compression deformation [J]. The Chinese Journal of Nonferrous Metals, 2006, 16(11): 1938–1944. (in Chinese)

[12] PRASAD Y V, GEGEL H L, DORAIVELU S M. Modeling of dynamic material behavior in hot deformation: Forging of Ti–6242 [J]. Metallurgical Transactions A, 1984, 15(10): 1883–1892.

[13] GEGEL H L, DORAIVELU S M. Modeling techniques used in forging process design [J]. ASM Handbook, 1988, 14(3): 417–438.

[14] BEHNOOD N, EVANS J T. Plastic deformation and the flow stress of aluminum–lithium alloys [J]. Acta Metallurgica, 1989, 37(2): 687–695.

[15] CAO X W, XU G F, DUAN Y L, YIN Z M, LU L Y, WANG Y J. Achieving high superplasticity of a new Al–Mg–Sc–Zr alloy sheet prepared by a simple thermal-mechanical process [J]. Materials Science and Engineering A, 2015, 647(5): 333–343.

[16] LI Bo, PAN Qing-lin, YIN Zi-min. Characterization of hot deformation behavior of as-homogenized Al–Cu–Li–Sc–Zr alloy using processing maps [J]. Materials Science and Engineering A, 2014, 614: 199–206.

[17] LUO J, LI M Q, MA D W. The deformation behavior and processing maps in the isothermal compression of 7A09 aluminum alloy [J]. Materials Science and Engineering A, 2012, 532(3): 548–557.

[18] SUN Y, HU L X, REN J S. Investigation on the hot deformation behavior of powder metallurgy TiAl-based alloy using 3D processing map [J]. Materials Characterization, 2015, 100(2): 163–169.

[19] LIU W, ZHAO H, LI D. Hot deformation behavior of AA7085 aluminum alloy during isothermal compression at elevated

- temperature [J]. Materials Science and Engineering A, 2014, 596(4): 176–182.
- [20] ZHANG H, LI L, YUAN D. Hot deformation behavior of the new Al–Mg–Si–Cu aluminum alloy during compression at elevated temperatures [J]. Materials Characterization, 2007, 58(2): 168–173.
- [21] LI B Q, PAN L, YIN Z M. Characterization of hot deformation behavior of as-homogenized Al–Cu–Li–Sc–Zr alloy using processing maps [J]. Materials Science and Engineering A, 2014, 614(1): 199–206.
- [22] SUN Y, HU L X, REN J S. Investigation on the hot deformation behavior of powder metallurgy TiAl-based alloy using 3D processing map [J]. Materials Characterization, 2015, 100(4): 163–169.
- [23] WANG Chun-xia, XU Fu-xiao, ZHAO Da-zhi, ZHAO Xiang, ZUO Liang. Hot deformation and processing maps of DC cast Al–15%Si alloy [J]. Materials Science and Engineering A, 2013, 577(11): 73–80.
- [24] YAN J, PAN P L, LI B, HUANG Z Q, LIU Z M, YIN Z M. Research on the hot deformation behavior of Al–6.2Zn–0.7Mg–0.3Mn–0.17Zr alloy using processing map [J]. Journal of Alloys and Compounds, 2015, 632(2): 549–557.
- [25] GHOLINIA A, HUMPHREYS F J, PRANGNELL P B. Production of ultra-fine grain microstructures in Al–Mg alloy by conventional rolling [J]. Acta Materialia, 2002, 50(5): 4461–4476.

## 热压缩过程中 Al–9Mg–1.1Li–0.5Mn 合金的流变应力和动态再结晶行为

陈喜红<sup>1,2</sup>, 范才河<sup>1</sup>, 胡泽艺<sup>1</sup>, 阳建君<sup>1</sup>, 高文理<sup>3</sup>

1. 湖南工业大学 冶金与材料工程学院, 株洲 412007;
2. 中国中车 株洲电力机车有限公司, 株洲 412004;
3. 湖南大学 材料科学与工程学院, 长沙 410082

**摘要:** 采用 Gleeble-3500 热模拟试验机对喷射成形 Al–9Mg–1.1Li–0.5Mn 合金挤压坯进行等温热压缩实验, 研究该合金在变形温度为 300–450 °C 和应变速率为 0.01–10 s<sup>-1</sup> 条件下的流变应力行为, 利用透射电镜(TEM) 和电子背散射技术(EBSD) 表征合金热压缩过程中的显微组织演变。结果表明, 变形参数对 Al–9Mg–1.1Li–0.5Mn 合金热压缩过程中流变应力和组织演变有非常显著的影响, 随着变形温度的降低和应变速率的升高, 峰值应力和稳态流变应力增加, 合金中的位错和亚结构数量增多; 反之, 随着变形温度的升高和应变速率的降低, 大角度晶界面积变大, 晶界呈锯齿状, 合金发生动态再结晶; 合金的组织呈纤维状, 合金在稳态变形阶段的主要软化机制为动态回复; 可用 Zener–Hollomon 参数的双曲正弦函数关系来描述合金的流变应力行为, 其变形激活能为 184.2538 kJ/mol; 热加图表明, 喷射成形 Al–9Mg–1.1Li–0.5Mn 合金挤压坯最合适的加工温度范围为 380–450 °C, 最佳应变速率范围为 0.01–0.1 s<sup>-1</sup>。

**关键词:** Al–9Mg–1.1Li–0.5Mn 合金; 流变应力; 本构方程; 加工图; 动态再结晶

(Edited by Bing YANG)